JOURNAL OF PROPULSION AND POWER
Vol. 23, No. 5, September–October 2007

Influence of Jet-Induced Transition on Separating Low-Pressure Turbine Boundary Layers

D. Reimann,* M. Bloxham,* K. L. Crapo,* J. D. Pluim,* and J. P. Bons†
Brigham Young University, Provo, Utah 84602

DOI: 10.2514/1.26677

Flow measurements were made on two highly loaded low-pressure turbine blade configurations in a linear cascade facility with and without the application of flow control. The L1M blade has a design Zweifel coefficient of 1.34 with a peak c_p near 47% c_x (midloaded) and the Pack B blade has a design Zweifel coefficient of 1.15 with a peak c_p at 63% c_x (aft-loaded). Flow and surface pressure data were taken for $Re_c = 20,000$ with 3% inlet freestream turbulence. For these operating conditions, a large separation bubble forms on the blade suction surface, beginning at 59% c_x and reattaching at 86% c_x on the L1M blade, with a nonreattaching bubble beginning at 68% c_x on the Pack B blade. Data were taken using a single-element hot-film anemometer. Higher-order turbulence statistics were used to identify transition and separation zones. Similar measurements were also made in the presence of unsteady forcing using pulsed vortex generator jets located 9% c_x upstream of the separation location. For the uncontrolled case, it was found that the separated laminar shear layer on the L1M blade started turbulent transition earlier than the Pack B but took longer to fully transition. This earlier transition appears to be a significant contributor to boundary-layer reattachment for the L1M blade. With the application of pulsed vortex-generating jets, the separation bubble was convected entirely off the blade for both blade configurations, but the Pack B bubble responded more slowly to the jet pulse due to a lower convection speed for the jet disturbance. Once the bubble was swept off of the L1M blade, a new bubble began to grow immediately. However, on the Pack B blade, there was a significant phase lag before bubble regrowth occurred.

Nomenclature

B	=	vortex-generating-jet blowing ratio, $U_{\text{jet}}/U_{\text{local}}$
c_p	=	pressure coefficient, $(P_{\text{Tin}} - P_{\text{local}})/(P_{\text{Tin}} - P_{\text{Sin}})$
c_x	=	blade axial chord
Re_c	=	Reynolds number based on cascade inlet conditions, $c_x U_{\text{in}}/\nu$
T	=	forcing period, 200 ms
t	=	time
U	=	velocity
u	=	instantaneous streamwise-velocity component
$\tilde{u}$	=	ensemble-averaged streamwise velocity
$\tilde{u}_{\text{max}}$	=	maximum ensemble-averaged velocity in the measurement domain
u_{mean}	=	mean streamwise-velocity component
u_{rms}	=	root mean square streamwise-velocity component
x	=	axial coordinate from the cascade inlet face
y	=	local surface-normal coordinate
z	=	spanwise coordinate
β	=	flow angle relative to the cascade axial direction
Γ	=	intermittency distribution
γ	=	intermittency
ν	=	kinematic viscosity

Subscripts

ex	=	cascade exit
in	=	cascade inlet
jet	=	vortex-generating jet
local	=	local freestream conditions
max	=	maximum value in the full cycle
S	=	static
T	=	total

Presented as Paper 2852 at the 3rd Annual Flow Control Conference, San Francisco, CA, 5–8 June 2006; received 20 July 2006; revision received 15 February 2007; accepted for publication 19 February 2007.

*Research Assistant, Mechanical Engineering. Student Member AIAA.
†Associate Professor, Mechanical Engineering, 435 Crabtree Technology Building; jbons@byu.edu. Senior Member AIAA.

I. Introduction

IN GAS turbines, separation is a major consideration for the efficient design of inlets and compressors. Because of the predominantly expanding flow downstream of the combustor, separation might not be considered to play as significant a role in turbine design. However, with the constant push to higher-stage loading and more aggressive turning angles, present and future turbine designs must insure healthy (attached) boundary layers for high aerodynamic efficiency. This is particularly the case in low-pressure turbines, for which several recent studies have reported dramatic increases in stage losses at a reduced blade-chord Reynolds number [1,2].‡ Sondergaard et al. [3] and Sharma [2] showed that this drop in efficiency at low Reynolds numbers can be attributed to boundary-layer separation on the blade suction surface. Predicting this separation and the subsequent transition and reattachment are still significant challenges for current design codes [4].

Boundary-layer separation is only a significant detriment to turbine-stage performance when the separation bubble does not reattach to the trailing edge of the blade. In this case, the total pressure loss in the wake increases dramatically and the enlarged wake width exacerbates unsteady losses associated with blade–wake interaction in the subsequent blade row [5]. Laminar-to-turbulent boundary-layer transition plays a critical role in determining reattachment. The added near-wall momentum associated with a turbulent boundary layer can often prevent boundary-layer separation altogether, even on some of the most aggressive loading profiles. As the flow Reynolds number drops (due to high-altitude or higher-temperature operation), the transition location moves further aft on the blade surfaces, reaching well into the diffusing portion of the passage. In such cases, boundary-layer separation may create a region of unsteady reverse flow beneath a separated laminar shear layer. If conditions are suitable, this laminar free shear layer will become unstable and transition to a turbulent shear layer. If this transition

‡Private communication with Dan Helton, 1997.

occurs with adequate suction surface remaining before the trailing edge, reattachment will likely occur. If not, the wake width may reach three–four times the width of the nonseparating airfoil [3].

The probability of boundary-layer reattachment is improved dramatically if the point of minimum pressure can be moved forward on the blade suction surface. In this way, separation occurs early enough to allow shear-layer transition and reattachment well before the trailing edge. Two recent studies by Praisner et al. [6] and Bons et al. both demonstrated the efficacy of this design strategy. The first study looked at two modified Pack B blade profiles: an aft-loaded derivative (Pack D-A) and a forward-loaded derivative (Pack D-F). In subsequent testing, Pack D-A experienced a dramatic increase in losses at $Re < 76,000$, whereas Pack D-F showed only minor loss increases down to $Re = 28,000$. Bons et al. [7] used a similar design strategy to develop a midloaded (L1M) blade profile that moved the peak c_p location from 63% c_x on the Pack B to 47% c_x on the L1M. Doing so insured a closed separation bubble on the L1M below $Re_c = 20,000$. The design Zweifel load coefficient for the L1M was 1.34, a 17% increase above the Pack B value (1.15). The design Zweifel load coefficient is defined as

$$Zw = 2\frac{S}{c_x}\sin^2\beta_{\text{ex}}\left[\frac{u_{\text{in}}}{u_{\text{ex}}}\cot\beta_{\text{in}} + \cot\beta_{\text{ex}}\right] \tag{1}$$

In Eq. (1), β_{in} and β_{ex} are the inlet and exit flow angles and u_{in} and u_{ex} are the inlet and exit axial velocities. As with any design strategy, forward loading has its limits. Compressibility effects in transonic stages may necessitate a more balanced loading profile to reduce shock losses. Also, even forward-loaded blades are expected to eventually reach their limit when the Zweifel load coefficient is pushed to values much above 1.34. Thus, Bons et al. [7] recommended combining loading optimization with active flow control techniques.

A number of recent studies summarized by Rivir et al. [8] have shown considerable promise in the arena of low-pressure turbine (LPT) separation reduction using embedded flow control devices. Rivir et al. reviewed progress with a wide variety of flow control devices including passive surface protrusions (delta wings) and recesses (dimples), microelectromechanical actuators, heated wires, electrostatic discharge devices, and vortex-generating jets (VGJs). Of the active control devices listed, VGJs are perhaps the most straightforward to implement in an engine, because the manufacturing technology required is virtually identical to that currently used for film cooling.

Experiments with VGJs, conducted in several low-speed turbine cascade facilities with the Pack B blade profile, have demonstrated substantial reductions in separation losses at low (separating) Reynolds numbers (25–65%, depending on flow conditions) [9–11]. VGJs are typically configured with a low pitch angle (30–45 deg) and aggressive skew angle (45–90 deg) to the near-wall flow direction. When operated in the steady mode, it has been shown that the VGJ creates a vortex pair with one very strong leg accompanied by a weak leg of opposite sign [11,12]. The result is a single, dominant, slowly decaying streamwise vortex that energizes the separating boundary layer by effectively bringing high-momentum freestream fluid near the wall. Experimental results have shown steady VGJs to be extremely robust, with effective operation over a wide range of flow conditions (Reynolds number and freestream turbulence) and control implementations (chordwise location and blowing ratio) [3,9].

Despite the success of steady VGJ flow control, the real promise for VGJ integration into a gas turbine engine is in the unsteady or pulsed mode. Laboratory tests indicate that the mass flow requirements of VGJs can be reduced to an almost negligible fraction (less than 0.01%) of the core mass flow through nonsteady forcing [9]. The flow mechanism responsible for pulsed VGJ separation control effectiveness is more complex than that for the steady control mode. An initial study of varying the jet duty cycle from 50 to 1% suggested that the fluid dynamics associated with the starting and ending of the jet are the most critical [9]. It was assumed that these transitions would be punctuated with vortical motions that would perform a comparable role to the streamwise vortices associated with steady VGJs. However, computational studies by Postl et al. [13] showed that although pulsed VGJs generated some freestream entrainment through vortex interaction, the primary mechanism for boundary-layer control was turbulent transition. They noted the presence of large-amplitude 2-D (spanwise) disturbances downstream of the VGJs that accelerated boundary-layer transition and thus reattachment. Bloxham et al. [14] subsequently used 3-D particle image velocimetry (PIV) measurements to show that although the VGJ event is clearly three-dimensional when it interacts with the upstream end of the separation bubble, its influence is approximately spanwise uniform by the time the separation bubble is pushed off the trailing edge of the blade. Once the jet had merged with the separation bubble, Bloxham et al. found little evidence of the vortical disturbances associated with steady control. Finally, Bons et al [15] explored the role of unsteady transition in contributing to the effectiveness of unsteady VGJs.

Flow control of separation is typically most effective when applied in the vicinity of the inception point to a large separation zone, such as in the nonreattaching case. In this case, a minimal amount of forcing (e.g., net mass flow for VGJs) can be leveraged to produce a substantial change in flow behavior. Indeed, the bulk of applications reported in the literature involve this type of control methodology [8–11]. The present study is intended to explore some of the differences between VGJ implementation with reattaching (closed) and nonreattaching (open) separations. Accordingly, phase-averaged and time-resolved flow measurements were made for both the midloaded L1M and aft-loaded Pack B blade profiles at low Reynolds numbers. Flow control was implemented in the unsteady mode, with particular attention given to the role of unsteady transition throughout the pulsing period.

II. Experimental Configuration

A detailed description of the cascade facility used for this study is found in Eldredge and Bons [11]. The open-loop wind tunnel is driven by a centrifugal blower and produces conditioned exit flow, with ±2% velocity uniformity and 0.3% freestream turbulence at the cascade inlet. For the present study, this level of background freestream turbulence was augmented to 3%, with a passive square-bar grid located five axial chords c_x upstream of the cascade. This level of turbulence more accurately reflects the conditions that would be found in an embedded blade row, similar to a low-pressure turbine stage. At the cascade inlet plane, the freestream turbulence was fairly isotropic (all three fluctuating velocity components within ±10%) and had an integral length scale of 2 cm. Acceleration in the blade passage causes the turbulence level to decay to below 2% at the exit, whereas the integral length scale increases to nearly 3 cm at the cascade exit plane.

The VGJ-equipped blade is located at the inner corner of the two-passage cascade so that the suction surface will experience uncovered turning as it would in a full linear cascade. Fourteen 0.64-mm-diam pressure taps were drilled into the suction surface of the inner blade, with seven on the pressure surface of the middle blade. These static pressure taps are used for verification of the c_p distribution in the controlled passage. All c_p and velocity data were taken over the center 0.15 m of the blade span, for which the flow was confirmed to be approximately two-dimensional. The inlet bleeds and exit tailboards of the cascade can be adjusted to produce nominally periodic flow through the two passages. Eldredge and Bons [11] showed that proper adjustment of these tunnel walls allowed the two-passage cascade to closely match both the c_p distribution and the boundary-layer behavior of the larger eight-blade Pack B linear cascade used by Sondergaard et al. [3].

Two blade profiles are used in the current study: the L1M and the Pack B. The midloaded L1M turbine blade was designed by Clark [16], using the recently implemented design and analysis system for turbine airfoils at the U.S. Air Force Research Laboratory. The blades have an axial chord c_x of 0.22 m and a span of 0.38 m. The cascade solidity (axial chord/spacing) is 0.99 and the design Zweifel load coefficient for the L1M is 1.34. The L1M has a closed separation bubble at least down to $Re_c = 20,000$. Pack B, a Pratt and Whitney

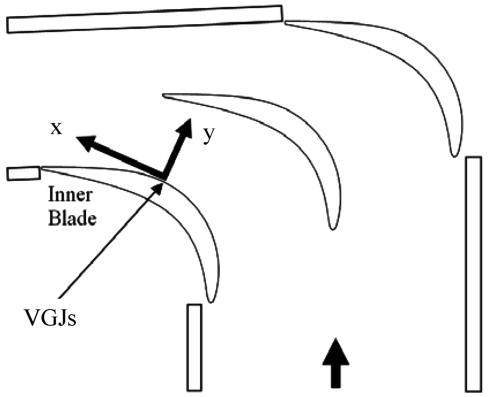

Fig. 1 Linear cascade facility. (shown with Pack B blades)

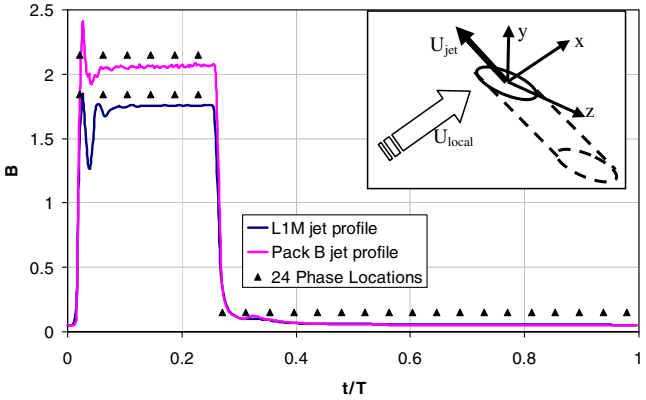

Fig. 2 VGJ exit velocity history with phase locations marked.

research blade design, is aft-loaded with $c_x = 0.238$ m and a span of 0.38 m. The design cascade solidity is 1.13 and the design Zweifel load coefficient is 1.15. The inside corner blade in the cascade (see Fig. 1) was also configured with a single row of 2.3-mm-diam VGJ holes on the L1M (2.6-mm diameter on the Pack B), spaced 10 hole diameters apart. The VGJs are located at 50% c_x on the L1M and at 59% c_x on the Pack B. The different VGJ locations were selected to be near the predicted peak c_p location for the respective blades. The holes were drilled with a 30-deg pitch angle to the blade surface and injected at a 90-deg skew angle from the streamwise direction. The pitch angle lies in the y–z plane and the skew angle lies in the x–z plane (see Fig. 2 inset). A pressurized cavity in the center of the blade provides for both steady and pulsed-jet operation over a range of blowing ratios.

The primary tool for flow diagnostics was a single-element hot-film anemometer mounted to a three-axis traverse located atop the cascade. The hot-film element has a diameter of 50.8 μm, a length of 1.02 mm, and a maximum frequency response of roughly 200 kHz. The traverse incorporated a blade-following device that allowed data to be taken at a constant wall distance spanning most of the blade suction surface (from 30% c_x to the blade trailing edge). The follower was used to obtain 15 streamwise profiles with wall distances approximately evenly spaced from 1.5 to 20 mm for the L1M. Seventeen streamwise profiles were obtained with wall distances approximately evenly spaced between 1.8 to 20 mm for the Pack B. The uncertainty in velocity was $\pm 1.5\%$ and the follower position was accurate to within ± 0.2 mm. Each profile consisted of 61 streamwise measurement locations for the L1M and 50 streamwise measurement locations for the Pack B, with a spacing ranging between 2.7 and 6.9 mm, the smaller steps concentrated in the region of the separation bubble. Flow data were acquired for both no-control ($B = 0$) and pulsed-control cases. For pulsed actuation, the high-pressure-air line feeding the VGJ plenum was connected to a Parker–Hannefin pulsed valve. The valve was operated at a frequency of 5 Hz

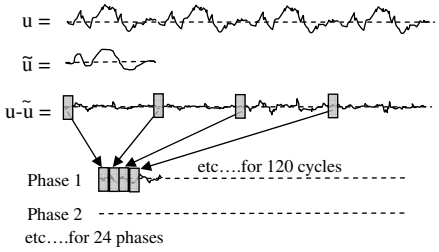

Fig. 3 Data processing flowchart for phase-locked unsteady velocity data.

with a duty cycle of 25%, the same conditions studied by Bons et al. [9]. The pulse of air exiting the jet holes is essentially a step function. Some attenuation occurs in the jet plenum, resulting in a slightly modified jet waveform, as shown in Fig. 2. This figure shows the jet-hole-exit blowing-ratio time history, as measured with a single-element hot film positioned at the jet exit (with no freestream flow). The $t/T = 0$ station represents the time at which the control signal was sent to the pulsed valve. The peak values of blowing ratio B were approximately 1.8 for the L1M and 2.1 for the Pack B.

III. Data Processing

Because the goal of this study was to document transition-related phenomena, large data records were taken at each position to assure steady statistics. For the no-control case, this was done using a sampling rate of 10 kHz for 16 s (160,000 data points). Flow intermittency γ was calculated using the methodology developed by Volino et al. [17], which employs both the first and second velocity derivatives as turbulence discriminators. The data are initially high-pass-filtered to eliminate low-frequency fluctuations that are common to both laminar and turbulent zones. Then the absolute value of the first derivative of velocity is compared with a predetermined threshold based on the local velocity fluctuations. This procedure yields a $\Gamma_1(t)$ distribution that is the first intermittency discriminator. A second discriminator $[\Gamma_2(t)]$ based on the absolute value of the second derivative of velocity is then coupled with the first discriminator to yield a final intermittency value. The composite result is low-pass-filtered to eliminate erratic transitions between the two states. The only modification that was made to the original Volino formulation was to calculate the high- and low- pass-filter frequencies using the local mean velocity rather than the local freestream velocity u_{local}. By doing this, the cutoff frequencies are more directly tied to the local convective speed of flow disturbances over the hot-film anemometer.

In addition to the mean and fluctuating velocity, higher-order turbulence statistics (skewness and kurtosis) were computed from each data record to provide multiple assessments of the turbulent character of the flow and to help identify the separated flow regimes. Skewness has been employed previously as a transition indicator in turbomachinery flows using surface-mounted heat flux gages [18]. Also, based on the work of Townsend [19], the kurtosis (or flatness) of the first derivative of the instantaneous velocity was computed as well.

In the case of pulsed flow control, the data acquisition time was increased to 24 s at the same frequency (10 kHz). The control signal from the pulsed valve controller was used to phase-lock the data acquisition with the pulsed VGJ control. To obtain the same turbulence statistics in the case of unsteady control, the data processing methodology shown schematically in Fig. 3 was followed. First, the 120 cycles (24 s × 5 Hz) of velocity data were averaged to produce an ensemble-averaged mean velocity distribution $\tilde{u}$ at each point. This ensemble was then subtracted from each of the 120 cycles to eliminate the bulk unsteady motion of the flow from the statistical calculations. The resulting velocity record represents cycle-to-cycle deviations from the ensemble-averaged mean flow. The next step was to divide each cycle into 24 phases of equal length (8.3 ms). The first phases of data from all 120 cycles were then concatenated to form a continuous velocity-deviation signal $(u - \tilde{u})$ associated with the first 8.3 ms of jet

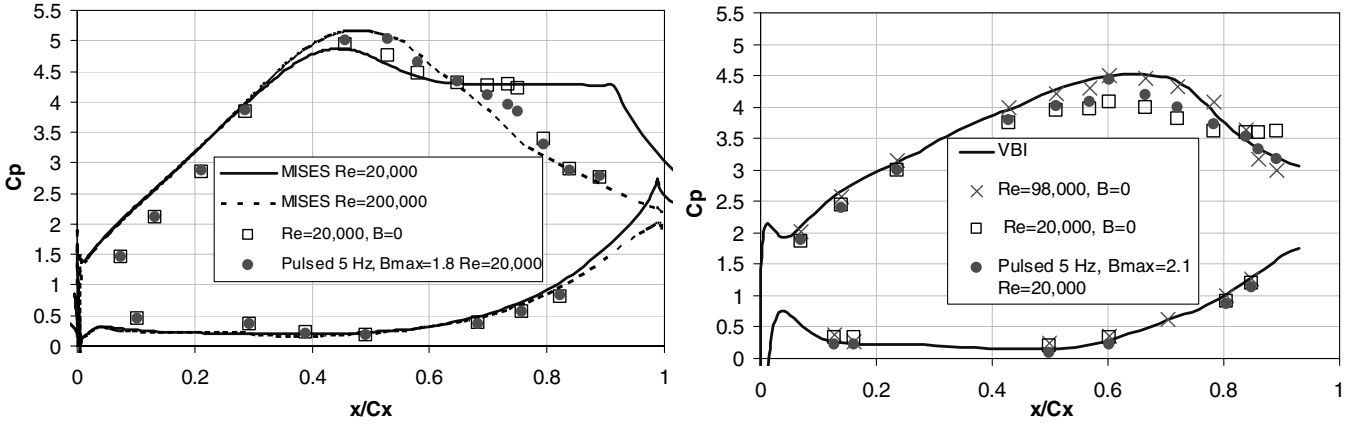

a) L1M **b) Pack B**

Fig. 4 Distributions of c_p for a) L1M at $B = 0$ and $B_{\max} = 1.8$ (5 Hz) at $Re_c = 20,000$ vs MISES predictions at $Re_c = 20,000$ and 200,000 b) Pack B at $B = 0$ and $B_{\max} = 2.1$ (5 Hz) at $Re_c = 20,000$ and $B = 0$ at $Re_c = 98,000$ vs VBI prediction.

actuation (a total of 10,000 data points). This data record was evaluated in a manner similar to that used with the no-control velocity data to determine intermittency, skewness, kurtosis, and kurtosis of $\mathrm{d}u/\mathrm{d}t$. The process was repeated for each of the 24 phases to produce the time variation of turbulent flow statistics and intermittency over one complete pulsing cycle.

IV. Results

The experimental pressure coefficient c_p distributions are presented in Figs. 4a and 4b for the L1M and the Pack B, respectively. Uncertainties in the experimental pressure measurements translate to an uncertainty of ± 0.10 in the c_p data at $Re_c = 20,000$. Figure 4a also contains a MISES prediction with and without separation (low and high Reynolds numbers, respectively) from Bons et al. [7]. In the low-Reynolds-number MISES prediction, forced transition (as specified by the Praisner and Clark [4] transition model) produced reattachment just before the blade trailing edge. For the L1M, the predicted separation zone is broader than that obtained experimentally, suggesting that the experimental transition location is earlier than expected. This is possibly due to the lower inlet turbulence level (0.5%) used in the calculation, compared with that used in the experiment (3%). Of significant note for this study is that the c_p data indicate reattached flow by 84% c_x, suggesting a closed

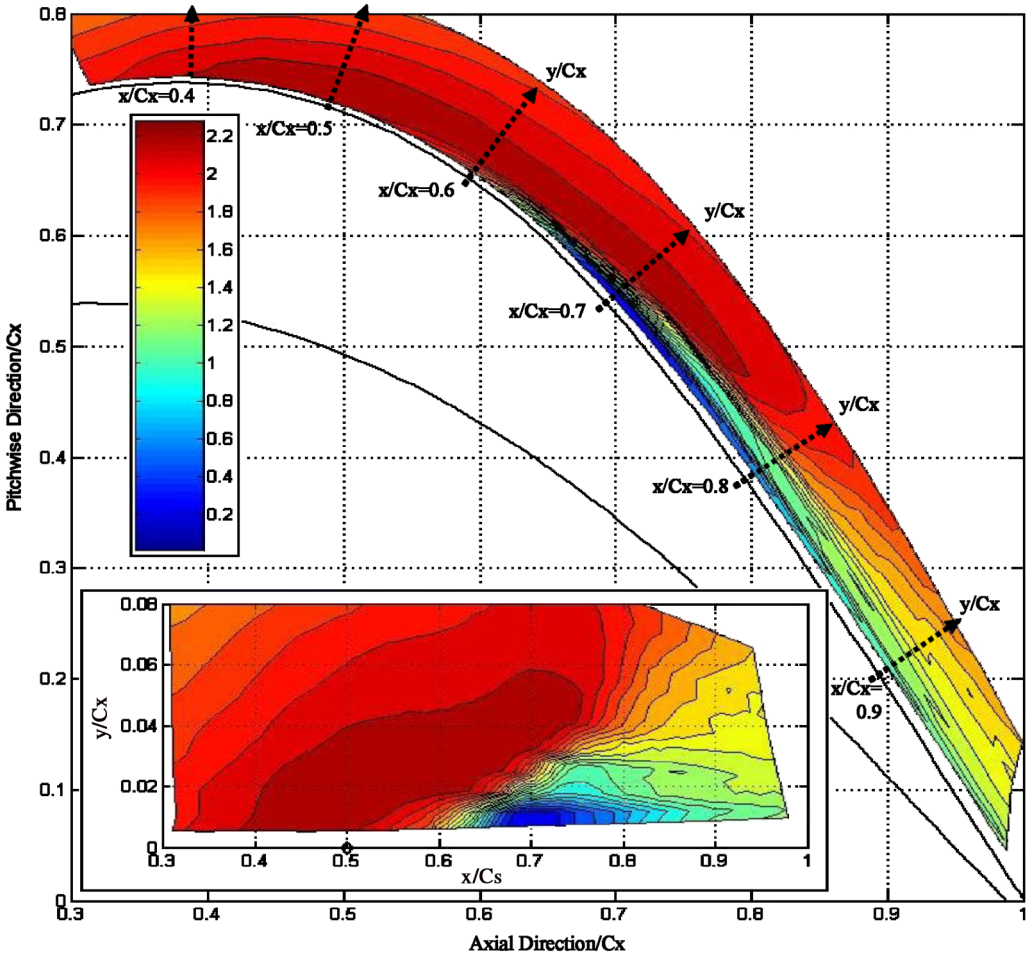

Fig. 5 Data of $u_{\mathrm{mean}}/U_{\mathrm{in}}$ for L1M with $B = 0$ presented in blade coordinates and in wall-normal axial chord coordinates.

separation bubble. With flow control, the c_p profile has a reduced separation zone and closely follows the nonseparating MISES calculation, particularly in the diffusing region of the blade (50–90% c_x). From this, it is clear that the pulsed VGJs are effective, in the time-averaged sense, at reducing laminar separation.

In addition to the experimental data, Fig. 4b includes a nonseparating vane–blade interaction (VBI) computational fluid dynamics prediction for the Pack B from Sondergaard et al. [3]. The aft loading of the Pack B is immediately evident in the later peak c_p location (63% c_x vs 47% for the L1M); c_p data are presented for both high and low Reynolds numbers without control and for low Reynolds numbers with flow control. Trailing-edge boundary-layer separation is evident in the low-Reynolds-number (no-control) case, with the last pressure tap at 90% c_x still indicating separated flow. The effect of this larger nonreattaching separation bubble is evident well upstream of the peak c_p location, as shown by the reduced c_p values compared with the high-Re_c case. Again, in the case with flow control, the separation is reduced and the blade performance improves markedly, indicating attached flow in a time-averaged sense.

A. Uncontrolled Case

Figure 5 shows the mean velocity data normalized by the inlet velocity ($u_{\text{mean}}/U_{\text{in}}$), as measured in actual blade coordinates around the L1M. The inset to Fig. 5 shows the same data with the y axis changed to the blade surface-normal distance normalized by c_x. The black arrows on the blade-velocity plot indicate the lines of constant x/c_x used to transform the blade plot into the more condense format. To make the presentation more compact and to more easily compare

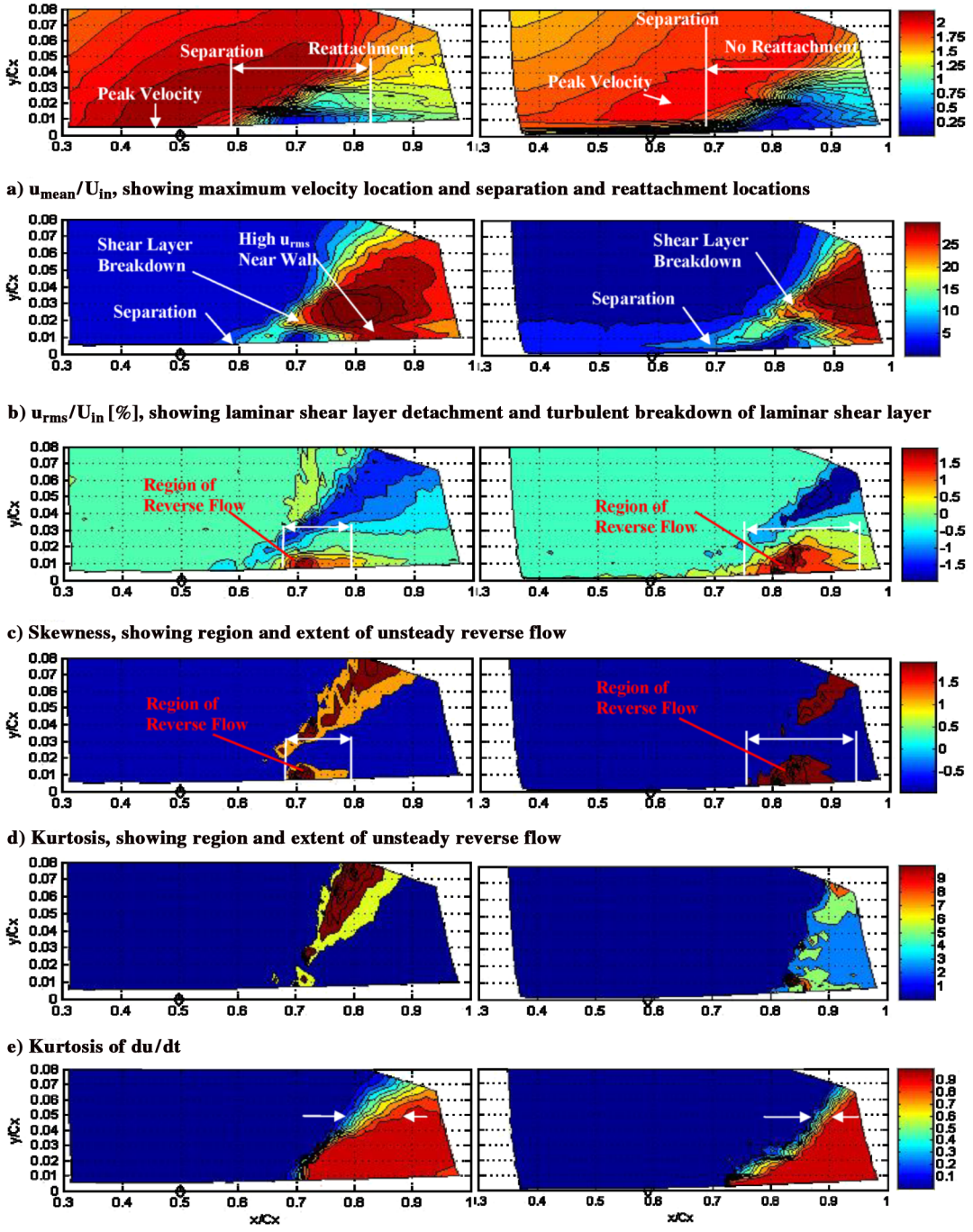

Fig. 6 No control ($B = 0$) at $Re_c = 20,000$: a) $u_{\text{mean}}/U_{\text{in}}$, b) $u_{\text{rms}}/U_{\text{in}}$ (%), c) skewness, d) kurtosis, e) kurtosis of du/dt, and f) intermittency.

data from the two blade cases side by side, the remaining plots are depicted in this condensed format. Accordingly, Fig. 6 shows the uncontrolled data for both the L1M and the Pack B cases. Figures 6a–6f include plots of: $u_{\text{mean}}/U_{\text{in}}$, $u_{\text{rms}}/U_{\text{in}}$, skewness, kurtosis, kurtosis of the acceleration, and the intermittency.

The first difference that can be seen in Fig. 6a is that the maximum velocity is well into the near-wall region of the L1M blade, but is removed from the wall in the Pack B case (maximum $u_{\text{mean}}/U_{\text{in}}$ locations are indicated on both plots). This more significant upstream influence of the separation zone in the Pack B data corroborates the c_p profile data shown in Fig. 4b. In the absence of a wall shear measurement to precisely identify the separation location, it was determined from Figs. 6a and 6b that the separation location for the L1M blade is near 59% c_x, whereas separation occurs near 68% c_x for the Pack B. This is identified in the plots by the region of rising near-wall u_{rms} accompanied by a sharp dropoff in u_{mean} that occurs as the boundary layer becomes a separated free shear layer. Incidentally, both of these separation locations are approximately 9% c_x downstream of the VGJ location for the respective blade design. Thus, the convective distance between the control point and the uncontrolled separation inception location is roughly equivalent in both cases. Sondergaard et al. [3] also identified the Pack B

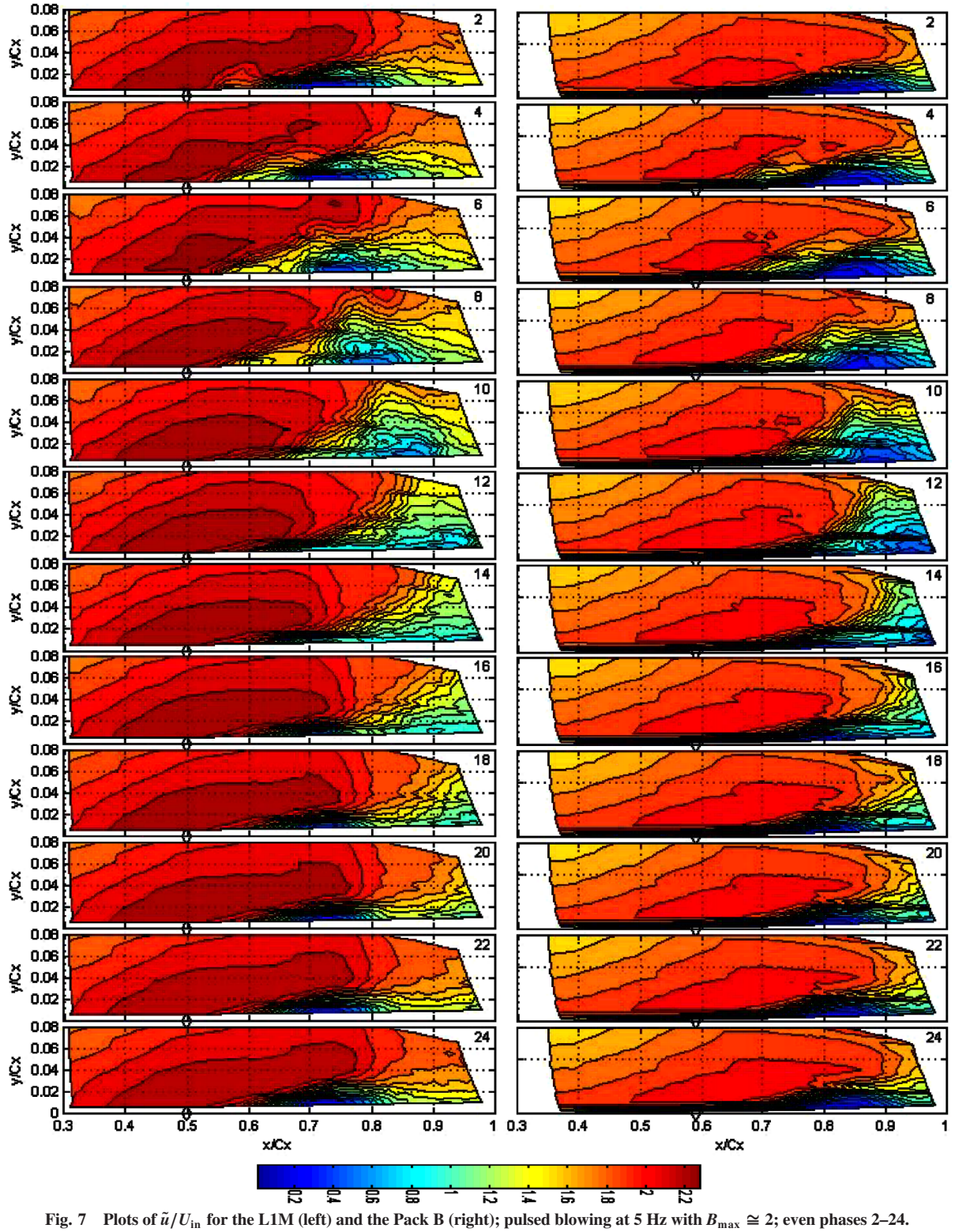

Fig. 7 Plots of $\tilde{u}/U_{\text{in}}$ for the L1M (left) and the Pack B (right); pulsed blowing at 5 Hz with $B_{\text{max}} \cong 2$; even phases 2–24.

separation location just before 70% c_x at Reynolds numbers below 40,000. No other research group has used the L1M profile yet, and so a comparison is not possible in that case. Following separation, the region of rising turbulence lifts away from the wall and forms a separated free shear layer above a region of unsteady reverse near-wall fluid. After a short distance, this laminar free shear layer begins to transition to a turbulent shear layer. The subsequent turbulent breakdown then spreads rapidly toward the wall in both cases. As identified on the plots, the separated shear layer from the L1M begins turbulent breakdown near 70% c_x, whereas breakdown occurs around 84% c_x for the Pack B. Based on these results, the laminar free-shear-layer extent is 11% c_x for the L1M (59% c_x separation to 70% c_x transition) and 16% c_x for the Pack B (68% c_x separation to 84% transition). The decreased transition length in the L1M case is likely due to the more aggressive deceleration of the mean flow noted in the c_p profile, given that adverse pressure gradients are known to be destabilizing. The peak level of turbulence in the turbulent shear layer reaches down to the nearest wall measurement location by 82% c_x for the L1M profile (as indicated in the plot), whereas the maximum turbulence level never penetrates down to the blade surface for the Pack B. It is thus concluded that the separated region successfully reattaches for the L1M around 82% c_x, whereas the Pack B separation does not fully reattach in the measurement domain.

Regions of unsteady reverse flow can be detected as areas of positive skewness in the near-wall region of Fig. 6c. Because the hot film is only sensitive to velocity magnitude, any negative (reverse flow) velocities are positively justified, resulting in positive skewness values in regions of low or near-zero u_{mean}. Both the L1M and Pack B show regions of strong positive skewness beneath the separated free shear layer. The streamwise extent of this unsteady reverse-flow region is about 70% longer in the Pack B case compared with that of the L1M. Because the flow turning is not yet complete at this blade location, the extended streamwise bubble length causes the Pack B free shear layer to migrate further from the blade surface before breakdown (nearly 50% further than the L1M). As the shear layer reattaches to the blade, the skewness returns to zero values near the wall for the L1M profile. The same is not true for the Pack B data, again emphasizing that the Pack B boundary layer never fully reattaches within the data domain. This same region of reversed flow in the heart of the separation region also shows elevated levels of kurtosis (Fig. 6d).

Following the trajectory of the separating free shear layer and continuing out into the freestream are bands of strongly negative skewness, as seen in Fig. 6c. These regions are indicative of high-velocity flow punctuated by short bursts from lower-momentum laminar pockets. Thus, Cattanei et al. [18] used skewness as a method of identifying flow transition. Townsend [19] also recommended using the kurtosis of the acceleration as a method of determining transition. The higher-order kurtosis and the kurtosis of acceleration show elevated readings along the same location as the vicinity of negative skewness. As expected, these transition indicators suggest that the location of transition occurs in the region of the shear-layer breakdown, as mentioned previously and indicated in the plots (i.e., shear-layer transition at $x/c_x = 0.7$ and $y/c_x = 0.02$ on the L1M and at $x/c_x = 0.84$ and $y/c_x = 0.03$ on the Pack B). It is interesting to note that the width of the skewness, kurtosis, and the kurtosis of the acceleration bands is much larger in the L1M plots than for the Pack B, particularly in the freestream. This indicates that the flow is transitioning over a longer streamwise distance for the L1M than for the Pack B. Because the Pack B shear layer is further from the wall when it finally transitions, the evolution to a fully turbulent character is perhaps less influenced by the proximity of the wall. Thus, even though the Pack B laminar shear layer convects further downstream before beginning to transition, it appears to transition more rapidly. The intermittency indicator plotted in Fig. 6f agrees well with the transition location suggested by Figs. 6c, 6d, and 6e.

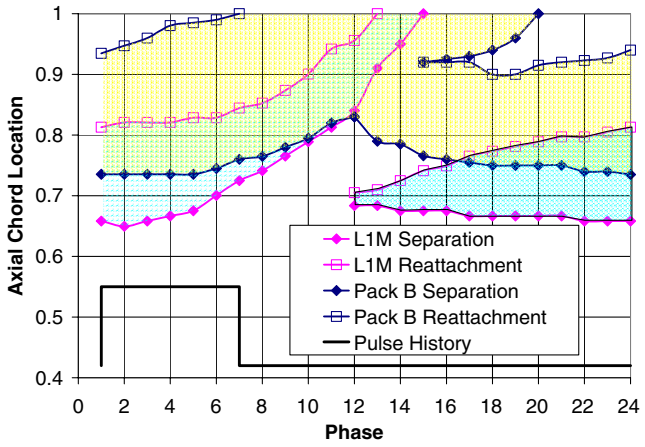

a)

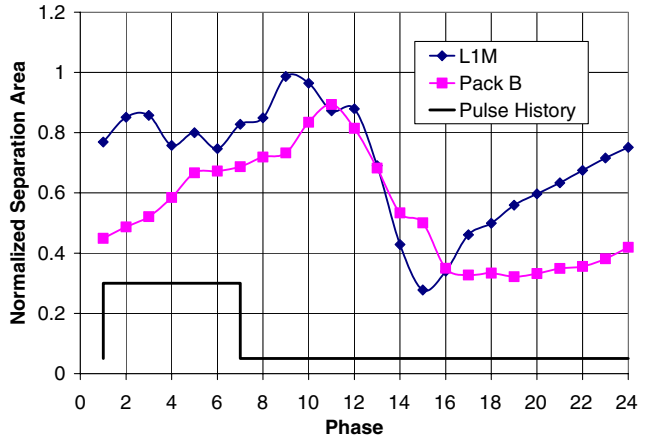

b)

Fig. 8 Separation-bubble evolution (defined as region in which $\tilde{u} < 0.4\tilde{u}_{\max}$ in Fig. 7) vs pulsing phase for the L1M and the Pack B: a) separation-bubble maximum upstream and downstream extent and b) integrated separation-bubble area normalized by bubble size with no control ($B = 0$).

B. Controlled Case

As mentioned previously, three-dimensional PIV data taken by Bloxham et al. [14] in the same cascade facility indicated that although the VGJ event is clearly three-dimensional when it interacts with the upstream end of the separation bubble, its influence is approximately spanwise uniform by the time the separation bubble is pushed off the trailing edge of the blade. Also, the same PIV data taken over a full hole pitch showed that the initial jet trajectory was approximately identical for the two blades up to the location in which it impacted the bubble. As such, the unsteady follower data with pulsed VGJs is presented for only one spanwise location (approximately two jet diameters above the upper lip of a VGJ hole near the blade midspan). Because the jet injection direction is upward along the span, the data plane is in the direct path of the jet injection (only two jet diameters away from the injection point). Accordingly, the jet event figures prominently in the data presented herein. The jet-hole-exit velocity profile in Fig. 2 indicates the locations of the 24 phases used to analyze the unsteady data. Figure 7 shows a series of ensemble-averaged $\tilde{u}/U_{\text{in}}$ contour plots for the 12 even-numbered phases for both the L1M and Pack B data.

As in the uncontrolled case (Fig. 6), ensemble-averaged peak velocities in Fig. 7 penetrate down closer to the wall for the L1M blade than they do for the Pack B. For both cases, the jet pulse causes an initial bunching up of the separation region, followed by its eventual ejection off the back of the blade. This evolution of the perturbed separation bubble is summarized in Fig. 8 using the ensemble-averaged velocity data in Fig. 7. Figure 8a shows the upstream and downstream extent of the separation bubble in the axial chord direction as a function of phase for each blade profile. The

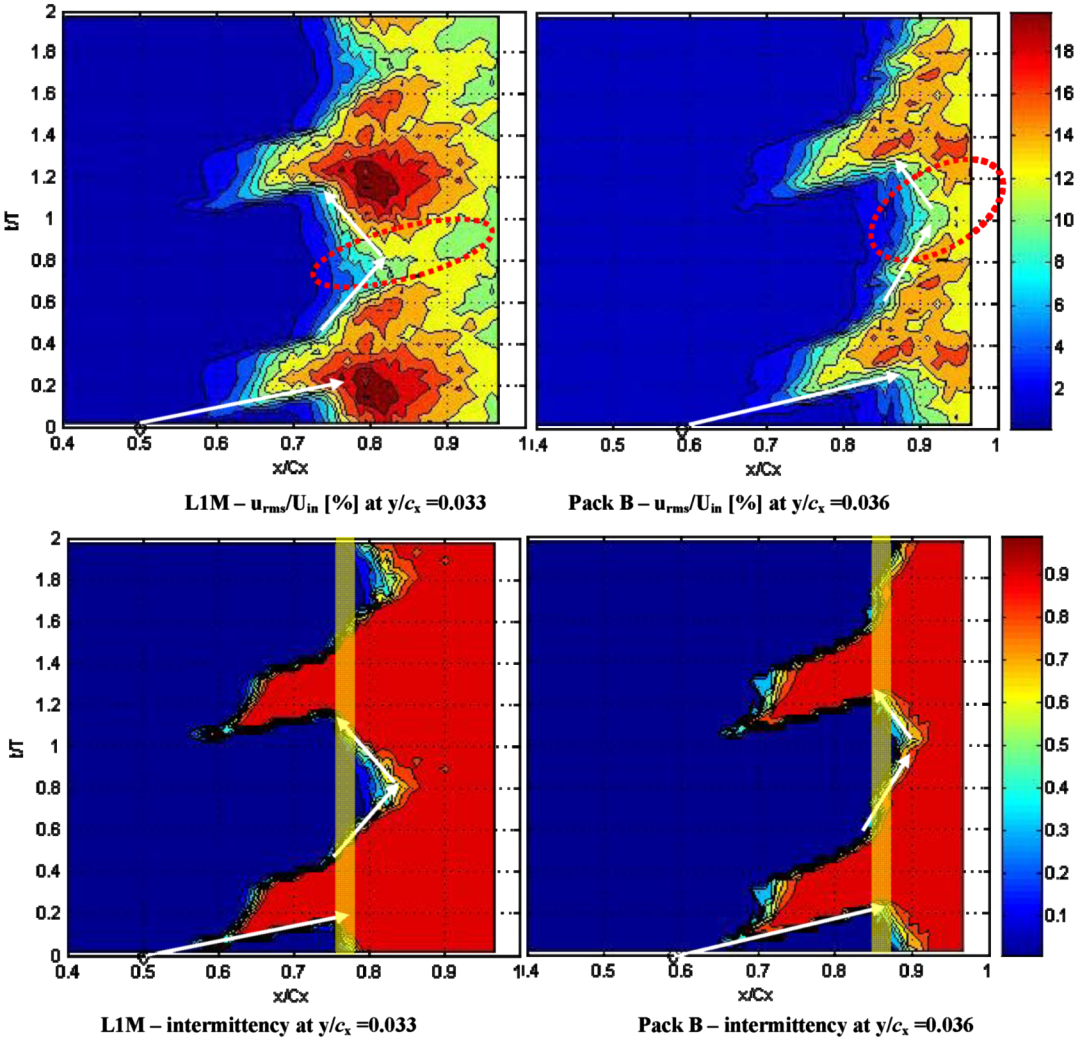

Fig. 9 Time–space plots of u_{rms}/U_{in} and intermittency for the L1M and the Pack B; the vertical band indicates the transition location without control ($B = 0$) at this y/c_x elevation (see Fig. 6f).

L1M bubble data are dark between the furthest upstream and downstream extents, and the Pack B bubble data are light. For purposes of this plot, the separation zone is defined as any region of the flow with less than 40% of the peak velocity in the measurement domain. The pulse history is shown along the bottom of the plot so that the response of the separation bubble can be tied directly to the control initiation and termination events. Essentially, the VGJ pulse causes a disturbance at the leading edge of the bubble that ultimately pushes the separation region off the back of the blade. In both cases, some residual separated flow remains on the blade after the bulk of the bubble is ejected, and this residual grows to form a new separation bubble until impacted by the next jet pulse. As seen in Fig. 8a, the mean trajectory of the L1M bubble displacement is steeper during its migration off the back of the blade. This is due to the higher freestream velocity present in the L1M passage that is sweeping the low-momentum fluid with it off the blade. After the separation bubble gets pushed off the back of the blade, the residual separation centered near 71% c_x continues to grow until the next jet pulse arrives. The Pack B bubble responds more slowly to the jet pulse, due to the reduced convective velocity of the jet disturbance and the larger separation bubble at the time of jet impact. Once the separation zone has been swept off the blade, new separation growth is centered around 82% c_x, expanding quickly to its former streamwise extent. In both cases, the streamwise extent of the bubble decreases in response to the injected jet, because the upstream end is effected before the downstream end. Thus, the bubble bunches up, becoming thicker in the blade-normal direction, before being convected off the blade.

Although Fig. 8a provides a measurement of the maximum streamwise extent of the separation zone, it is apparent from Fig. 7 that the low-momentum regions on the two blades have different wall-normal "thicknesses" as well. For instance, though the bubble regrowth (phases 16–24) on the Pack B has a longer streamwise extent than the L1M, it is much thinner and thus contains less stagnant fluid. One way to characterize this change in separation-bubble shape is to integrate the low-momentum area as a function of phase (Fig. 8b). In this plot, the integrated separation size is normalized by the separation-bubble size without control ($B = 0$) for both the L1M and Pack B cases. Thus, a normalized separation area of unity represents no change in bubble size from the no-control baseline case. As in Fig. 8a, the separation zone is defined as the region of the flow with less than 40% of the peak velocity. An initial observation from Fig. 8b is the overall level of control offered by VGJs for the different cases. The average reduction in separation area for the Pack B is roughly 50%, whereas the L1M data hover around 0.85 (only 15% net reduction) for over half of the pulsing cycle. Because the uncontrolled separation is 2.5 times larger in area on the Pack B than on the L1M, the controlled L1M data still have less separation area; however, the percent reduction in area is significantly less than the Pack B. To interpret the trends in Fig. 8b, it must be remembered that the L1M separation bubble is centered much further upstream from the trailing edge than the Pack B separation bubble. Consequently, during phases 1–6, the L1M separation is being convected downstream without any significant change in size. From phases 6–10, the L1M separation bunches up, as indicated earlier, producing a sharp increase in size

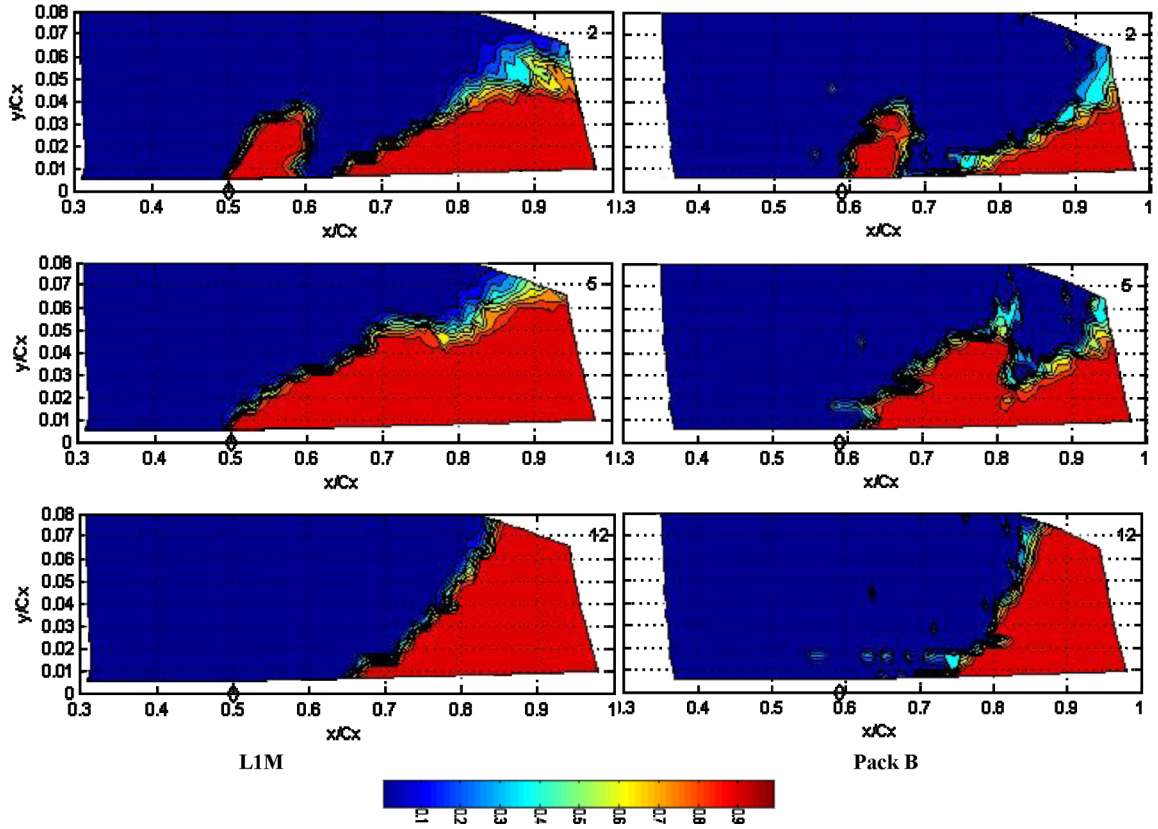

Fig. 10 Intermittency plots for the L1M (left) and the Pack B (right) at phases 2, 5, and 12.

(even reaching the no-control size at one point). After phase 12, the rounded separation zone begins to convect out of the measurement domain and off the blade, thus the precipitous drop in separation size. The minimum reduction in size is approximately 70%. Following this, the bubble regrowth is approximately linear until phase 2, just before the next pulse impacts the bubble leading edge.

The Pack B data show a very different bubble response in Fig. 8b. First, when the jet is turned on, the bubble size is still growing unimpeded. By phase 6, the effects of the jet become evident because the bubble growth slows somewhat. This slower response was noted in Fig. 8a and is due to the slower convection speeds in the Pack B cascade. The bubble grows to within 90% of its no-control size before exhibiting a monotonic decrease from phases 11 to 16. The bubble reduction is more gradual compared with the L1M case, though it eventually reaches the same minimum point (∼0.3) at roughly the same phase. Following this, there is a lagged response from phases 16 to 22 wherein the bubble size does not change. Not until phase 23 does the linear growth rate begin with roughly the same slope as with the L1M. The growth continues until the effect of the next pulse becomes apparent again in phase 6. This lagged response from phases 16–22 is a characteristic noted previously by Bons et al., [9] and is clearly not a characteristic of reattaching separation bubbles (e.g., the L1M). Apparently, the large-amplitude flow oscillations associated with the ejection of a nonreattaching separation bubble create a temporary flow inertia that maintains the attached state for some finite period of time (50 ms in this case) after the separation has been eliminated and the control is off.

The unsteady jet interaction with the separation bubble can also be viewed in a time–space plot (Fig. 9). A similar presentation was used by Volino et al. [10] for their synthetic jet data. Figure 9 shows the ensemble-averaged turbulence and intermittency over two jet cycles at a constant wall distance for both blade configurations ($y/c_x \cong 0.033$ for the L1M and $y/c_x \cong 0.036$ for the Pack B). Recall that in this case, u_{rms} is the unsteadiness that remains after the bulk unsteady motion $\tilde{u}$ corresponding to the 5-Hz pulsing of the jets has been removed (see Fig. 3). The trajectory of the jet initiation is noted (with white arrows) as the lower edge of the elevated turbulence and intermittency band emanating from the jet hole at 50% c_x (for the L1M) and 59% c_x (for the Pack B). The average convection velocity of the jet disturbance is roughly 70% of the local freestream velocity for the L1M case and 85% for the Pack B. The distance required for the jet to penetrate from the wall to the elevation shown in the figures is approximately 15% c_x in both cases. The jet-termination event convects at approximately the same velocity until it is engulfed in the separation-bubble dynamics near the uncontrolled ($B = 0$) transition location (highlighted with a vertical band).

In the L1M case, the termination event merges with a very active separation zone at $x/c_x = 0.74$ and $t/T = 0.4$. After this, the line of transition (and elevated u_{rms}) decelerates to roughly 20% of the average local velocity (indicated by the arrow). This deceleration occurs as the separation bubble is being pushed off the blade, and the residual bubble is being thinned until it almost disappears from this y/c_x level by $t/T = 0.75$. Between $t/T = 0.75$ and 0.85, there is a brief lull in turbulent activity that bears some resemblance to the "calmed zones" following convected wake disturbances noted by Gostelow and Thomas [20] and Stieger and Hodson [21] (noted in Fig. 9 with an oval) [20,21]. The calmed zone is typically marked by low turbulence levels and laminarlike boundary-layer behavior. Following this, a resurgence of the separation bubble redirects the transition line back upstream to the uncontrolled ($B = 0$) transition location at approximately the same velocity. The Pack B time–space plots show a similar behavior, though the calmed region is larger, due to the phase lag in bubble regrowth, as noted in Fig. 8b.

A more complete picture of the transition dynamics can be made with the aid of the phase-locked intermittency plots of Fig. 10. This figure shows the intermittency characteristics of the flow for both blade profiles at phases 2, 5, and 12. At phase 2, the jet has just been initiated and its influence on the local flow transition can clearly be seen. This region of transitioned flow is convected downstream at a higher velocity on the L1M blade, thus by phase 5, it has already combined with the downstream region of separation-induced transition. For the Pack B, the jet-induced transition has not yet completely merged with the downstream region of transition by

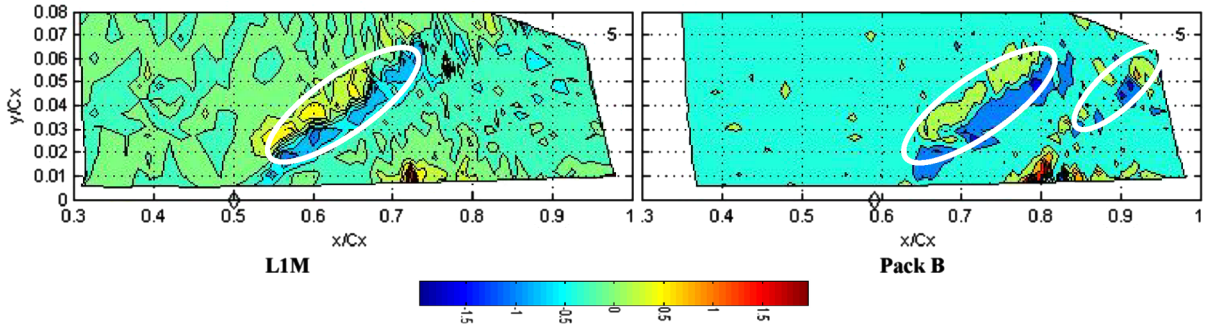

Fig. 11 Skewness plots for the L1M (left) and the Pack B (right) at phase 5. Transition regions of positive/negative skewness identified by ovals.

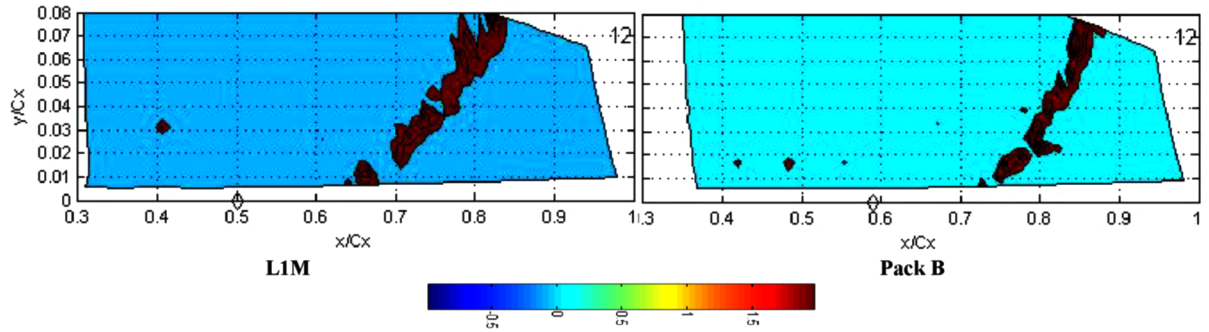

Fig. 12 Kurtosis plots for the L1M (left) and the Pack B (right) at phase 12.

phase 5. After the jets are turned off, the transition migrates downstream. Just as the separation bubble bunches up before it is ejected, the line of transition also appears to bunch up, as seen by the steeper slope of the transition region in phase 12 of Fig. 10. After the separation region is ejected off the back of the blade, the slope of the transition line again decreases before the initiation of the next pulse. As with the uncontrolled data in Fig. 6, higher-order turbulence statistics can be used to corroborate the trends highlighted in the intermittency plots. Figures 11 and 12 show skewness and kurtosis plots at phases 5 and 12, respectively, for direct comparison with Fig. 10. The regions of negative skewness in Fig. 11 line up with the regions of transition indicated by the phase-5 intermittency plots. A single band of negative skewness identifies the merged jet and separation-induced transition lines for the L1M, and the two discrete bands of negative skewness for the Pack B indicate that the full impact of the jet influence has not yet reached the downstream region of transition. Also, the kurtosis plots at phase 12 (Fig. 12) show the steeper transition line slope highlighted previously in Fig. 10.

V. Conclusions

Hot-film measurements were taken in a low-speed, low-pressure turbine cascade to obtain detailed unsteady velocity and turbulence data in two separating boundary layers. Data were taken for two different blade profiles, a midloaded L1M and an aft-loaded Pack B design, under both pulsed VGJ controlled and no-control conditions. Comparisons were made between the separation characteristics and control characteristics and separation regrowth for each set of blades. Flow separation characteristics differed for the midloaded L1M (which had a separating, reattaching boundary layer) and the aft-loaded Pack B (which had a separating, nonreattaching boundary layer). Without flow control, the separating laminar shear layer on the Pack B remained stable for nearly twice as long as on the L1M before experiencing turbulent breakdown. Because of the delayed shear-layer transition, the Pack B separation did not fully reattach to the blade, unlike the L1M. Separation control for the L1M showed significantly less benefit (in terms of bubble-size reduction) due to the upstream location of the bubble. Once the bubble was swept off, separation regrowth began immediately until the jet pulsing cycle restarted. For the Pack B blade, bubble regrowth was not evident for nearly 35% of the pulsing cycle after the separation bubble had been convected off the blade. This may be due to the increased flow inertia caused by the large-amplitude flow oscillations inherent with the control of large nonreattaching separations. These results suggest that the better-performing blade (L1M) is not necessarily the best candidate for flow control because it does not exhibit the phase-lag response that is characteristic of an open-bubble separation (Pack B). Thus, for maximum efficiency, the integration of flow control technology into gas turbines must be accomplished as an integral part of the design rather than as an add-on to enhance performance.

Acknowledgments

Financial support from the U.S. Air Force Office of Scientific Research is gratefully acknowledged, with Rhett Jefferies as program manager. Also, advice and guidance received from John Clark and Rolf Sondergaard at the U.S. Air Force Research Laboratory during this effort is greatly appreciated.

References

[1] Matsunuma, T., Abe, H., Tsutsui, Y., and Murata, K., "Characteristics of an Annular Turbine Cascade at Low Reynolds Numbers," IGTI 1998, Stockholm, Sweden, American Society of Mechanical Engineers Paper 98-GT-518, 1998.

[2] Sharma, O., "Impact of Reynolds Number on LP Turbine Performance," 1997 Minnowbrook 2 Workshop on Boundary Layer Transition in Turbomachines, NASA CP-1998-206958, 1998.

[3] Sondergaard, R., Bons, J. P., and Rivir, R. B., "Control of Low-Pressure Turbine Separation Using Vortex Generator Jets," *Journal of Propulsion and Power*, Vol. 18, No. 4, July–Aug. 2002, pp. 889–895.

[4] Praisner, T. J., and Clark, J. P., "Predicting Transition in Turbomachinery, Part 1: A Review and New Model Development," American Society of Mechanical Engineers Paper GT-2004-54108, 2004.

[5] Denton, J. D., "Loss Mechanisms in Turbomachines," *Journal of Turbomachinery*, Vol. 115, Oct. 1993, pp. 621–656.

[6] Praisner, T. J., Grover, E. A., Rice, M. J., and Clark, J. P., "Predicting Transition in Turbomachinery, Part 2—Model Validation and

Benchmarking," American Society of Mechanical Engineers Paper GT-2004-54109, 2004.
[7] Bons, J. P., Hansen, L. C., Clark, J. P., Koch, P. J., and Sondergaard, R., "Designing Low-Pressure Turbine Blades with Integrated Flow Control," Turbo Expo 2005: Power for Land, Sea, and Air, American Society of Mechanical Engineers Paper GT2005-68962, 2005.
[8] Rivir, R. B., Sondergaard, R., Bons, J. P., and Lake, J. P., "Passive and Active Control of Separation in Gas Turbines," Fluids 2000, Denver CO, AIAA Paper 2000-2235, 2000.
[9] Bons, J. P., Sondergaard, R., and Rivir, R. B., "The Fluid Dynamics of LPT Blade Separation Control Using Pulsed Jets," *Journal of Turbomachinery*, Vol. 124, No. 77, Jan. 2002, pp. 77–85.
[10] Volino, R. J., "Separation Control on Low-Pressure Turbine Airfoils Using Synthetic Vortex Generator Jets," Turbo Expo 2003: Power for Land, Sea, and Air, American Society of Mechanical Engineers Paper GT2003-38729.
[11] Eldredge, R. G., and Bons, J. P., "Active Control of a Separating Boundary Layer with Steady Vortex Generating Jets—Detailed Flow Measurements," 42nd AIAA Aerospace Sciences Meeting and Exhibit, Reno, NV, AIAA Paper 2004-751, 2004.
[12] Hansen, L. C., and Bons, J. P., "Time-Resolved Flow Measurements of Pulsed Vortex-Generator Jets in a Separating Boundary Layer," 2nd AIAA Flow Control Conference, Portland, OR, AIAA Paper 2004-2203, 2004.
[13] Postl, D., Gross, A., and Fasel, H. F., "Numerical Investigation of Low-Pressure Turbine Blade Separation Control," AIAA Paper 2003-0614, 2003.
[14] Bloxham, M., Reimann, D., and Bons, J. P., "The Effect of VGJ Pulsing Frequency on Separation Bubble Dynamics," *44th AIAA Aerospace Sciences Meeting and Exhibit, Reno, NV*, AIAA Paper 2006-0876, 2006.
[15] Bons, J. P., Bloxham, M., and Reimann, D., "Separated Flow Transition on an LP Turbine Blade with Pulsed Flow Control," 2006 IGTI Conference, Barcelona, Spain, American Society of Mechanical Engineers Paper GT2006-90754, 2006.
[16] Clark, J. P., "An Integrated Design, Analysis, and Optimization System for Turbine Airfoils," U.S. Air Force Research Lab., Rept. , Wright–Patterson AFB, OH, 2004.
[17] Volino, R. J., Schultz, M. P., and Pratt, C. M., "Conditional Sampling in a Transitional Boundary Layer Under High Freestream Turbulence Conditions," *Journal of Turbomachinery*, Vol. 125, No. 28, 2003, pp. 28–36.
[18] Cattanei, A., Zunino, P., Schroder, T., Stoffel, B., and Matyschok, B., "Detailed Analysis of Experimental Investigations on Boundary Layer Transition in Wake Disturbed Flow," 2006 IGTI Conference, Barcelona, Spain, American Society of Mechanical Engineers Paper GT2006-90128, 2006.
[19] Townsend, A. A., "Local Isotropy in the Turbulent Wake of a Cylinder," *Australian Journal of Scientific Research*, Series A, Vol. 1, 1948, pp. 161–174.
[20] Gostelow, J. P., and Thomas, R. L., "Response of a Laminar Separation Bubble to an Impinging Wake," Turbo Expo 2003: Power for Land, Sea, and Air, American Society of Mechanical Engineers Paper GT2003-38972, 2003.
[21] Stieger, R. D., and Hodson, H. P., "The Transition Mechanism of Highly Loaded LP Turbine Blades," Turbo Expo 2003: Power for Land, Sea, and Air, American Society of Mechanical Engineers Paper GT2003-38304, 2003.

T. Shih
Associate Editor